REFERENCE COPY
C. 2

SANDIA REPORT

SAND97–8567
Unlimited Release
Printed November 1997

Adhesion and Fracture of Tantalum Nitride Films

(*Acta Materialia*, in press)

N. R. Moody, R. Q. Hwang, S. Venkataraman, J. E. Angelo, D. P. Norwood, W. W. Gerberich

Prepared by
Sandia National Laboratories
Albuquerque, New Mexico 87185 and Livermore, California 94550

Sandia is a multiprogram laboratory operated by Sandia Corporation, a Lockheed Martin Company, for the United States Department of Energy under Contract DE-AC04-94AL85000.

Approved for public release; distribution is unlimited.

Sandia National Laboratories

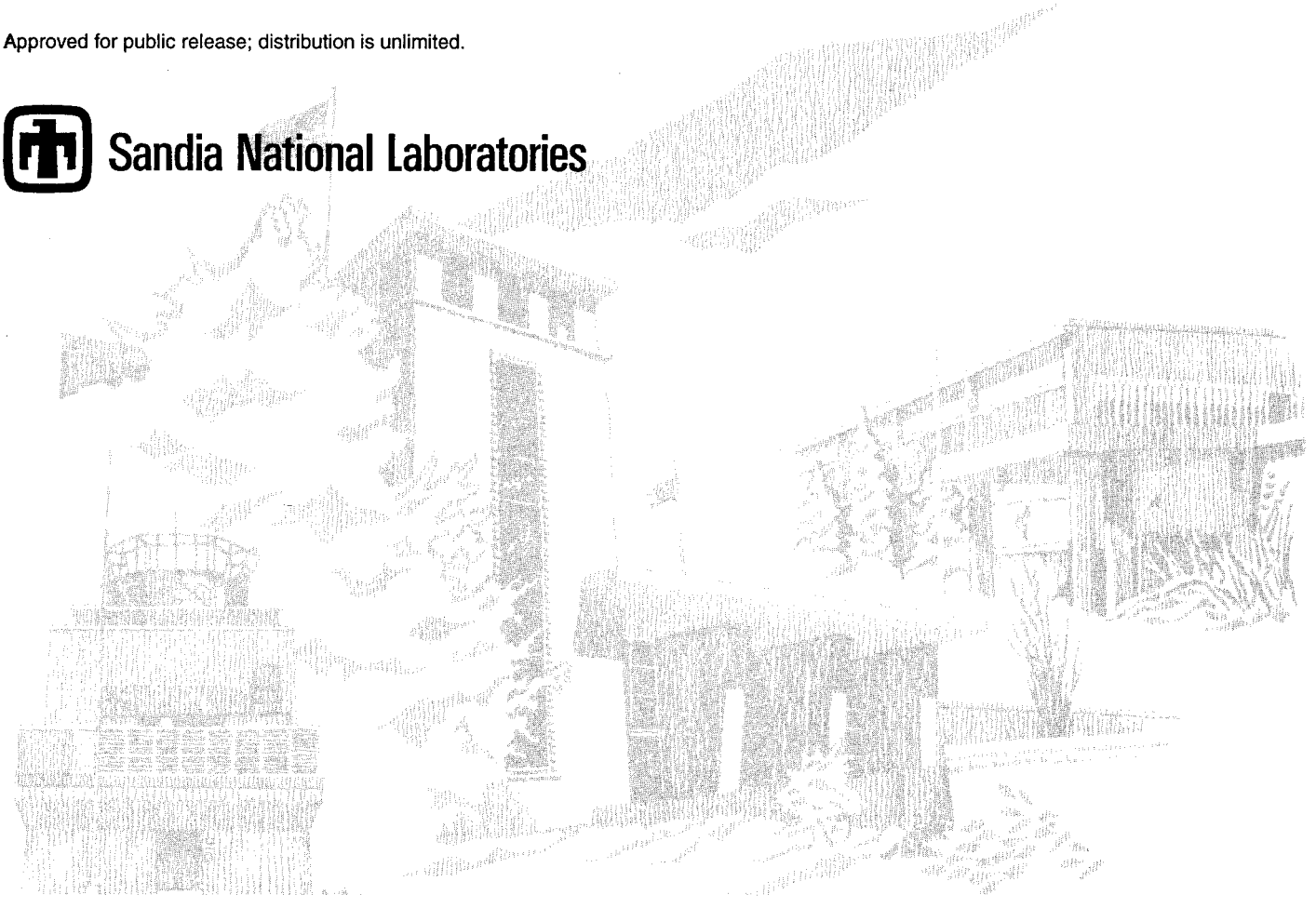

SF2900Q(8-81)

Issued by Sandia National Laboratories, operated for the United States Department of Energy by Sandia Corporation.
NOTICE: This report was prepared as an account of work sponsored by an agency of the United States Government. Neither the United States Government nor any agency thereof, nor any of their employees, nor any of their contractors, subcontractors, or their employees, makes any warranty, express or implied, or assumes any legal liability or responsibility for the accuracy, completeness, or usefulness of any information, apparatus, product, or process disclosed, or represents that its use would not infringe privately owned rights. Reference herein to any specific commercial product, process, or service by trade name, trademark, manufacturer, or otherwise, does not necessarily constitute or imply its endorsement, recommendation, or favoring by the United States Government, any agency thereof, or any of their contractors or subcontractors. The views and opinions expressed herein do not necessarily state or reflect those of the United States Government, any agency thereof, or any of their contractors.

Printed in the United States of America. This report has been reproduced directly from the best available copy.

Available to DOE and DOE contractors from
Office of Scientific and Technical Information
P.O. Box 62
Oak Ridge, TN 37831

Prices available from (615) 576-8401, FTS 626-8401

Available to the public from
National Technical Information Service
U.S. Department of Commerce
5285 Port Royal Rd
Springfield, VA 22161

NTIS price codes
Printed copy: A03
Microfiche copy: A01

SAND 97-8567
Unlimited Release
Printed November 1997

ADHESION AND FRACTURE OF TANTALUM NITRIDE FILMS

N. R. Moody
Materials Reliability Department
Sandia National Laboratories/California

R. Q. Hwang
Surface Chemistry Department
Sandia National Laboratories/California

S. Venkataraman
Applied Materials
Santa Clara, CA 94054

J. E. Angelo
Seagate Technologies
Bloomington, MN 55420

D. P. Norwood
Thin Film, Vacuum and Packaging Department
Sandia National Laboratories/New Mexico

and

W. W. Gerberich
University of Minnesota
Minneapolis, MN 55455

ABSTRACT

Indentation fracture and continuous nanoscratch testing were used in this study to determine the effects of compressive residual stresses on the fracture of thin sputter-deposited tantalum nitride films. Some films were tested in the as-deposited condition while others were vacuum annealed at 300°C. The only discernible change in structure was a surface rearrangement of atoms into parallel arrays of striations on the vacuum annealed samples revealing a high compressive residual stress state after deposition. Comparison of results and application of mechanics-based models showed that these stresses had a strong effect on the fracture of the as-deposited films. The models also provided a good measure of the residual stress levels and interfacial strain energy release rates.

ACKNOWLEDGMENTS

The authors thank C. Rood from Sandia National Laboratories, Livermore, CA and J. Nelson from the University of Minnesota for their technical support. We especially thank J. Hoehn and D. Bahr of the University of Minnesota and M. De Boer from Sandia National Laboratories, Albuquerque, NM for their many helpful technical discussions. N. R. Moody, R. Q, Hwang, D. P. Norwood, and J. E. Angelo gratefully acknowledge the support of the U.S. DOE through Contract DE-AC04-94AL85000. S. Venkataraman and W. W. Gerberich gratefully acknowledge the support of the Center for Interfacial Engineering at the University of Minnesota under grant NSF/CDR-8721551. W. W. Gerberich also acknowledges support of the U. S. DOE through Contract DE-FG02-96ER45574.

INTRODUCTION

Thin films are used in many applications where properties such as resistance to abrasion, corrosion, permeation and oxidation, or special magnetic and dielectric properties, are needed to insure performance and reliability. [1] In all of these applications, performance, reliability, and durability are tied directly to interface structure and composition. [1,2,3] Of particular interest are thin tantalum nitride films as they are used extensively in microelectronics applications because of their excellent long-term stability and low temperature coefficients of resistance. [4,5] They are sputter deposited which produces films with a high structural defect content and high compressive residual stresses both of which can alter the physical and mechanical properties of microelectronic thin films. [6,7] They are then air annealed at 300°C to improve stability and trim the resistors to within desired tolerance. [4,8] This procedure creates a surface oxide layer less than 8 nm thick but does not relieve the intrinsic compressive residual stresses.

Neither the contributions of interface structure and composition nor the superimposed effects of compressive residual stress on properties and the resistance of thin tantalum nitride films to interfacial fracture are well-defined due to limitations in test techniques. Traditional tests employ double-cantilever beam, asymmetric cantilever beam, notched three and four-point flexural beam [9,10] and thin film sandwich geometries. [11] They are based on fracture mechanics theory and provide good measures of strain energy release rates. However, the strain energies measured vary between each type of sample employed due to sample size and physical constraints.

As a result, we employed nanoindentation [12-15] and continuous nanoscratch testing [16-18] to determine the effects of the intrinsic compressive residual stresses on the properties and fracture resistance of the thin tantalum nitride films. These techniques sample small volumes of material while preserving the production configuration of a free surface. The indentation fracture tests are easy to perform and strain energy release rates can be determined from mechanics-based analyses. [19-21] However, the force that can be applied is limited in magnitude and extent. The continuous nanoscratch tests can apply a much greater force over a larger area in comparison with indentation tests but lack a rigorous derivation of stress distributions and strain energy release rates. [16-18] Nevertheless, good approximations for strain energy release rates can be obtained using blister and buckling solutions for systems where residual stresses dominate fracture behavior. [19-21] When combined with atomic force and high resolution transmission electron microscopy, the results define the relationships between structure, properties and interfacial fracture on a submicron scale.

MATERIALS AND PROCEDURE

Materials. In this study, thin tantalum nitride films were reactively sputtered onto smooth single crystal sapphire substrates using a d. c. magnetron sputtering unit. The substrates had been prepared by annealing at 1350°C in air. They were then transferred to the deposition chamber and heated to 170°C in vacuum for two hours to drive off moisture which was followed by an RF backsputter for 120 s to remove contaminants and expose fresh material. With a vacuum maintained to at least 1.3×10^{-5} Pa (10^{-7} torr), the films were deposited using a tantalum target, argon as a carrier gas, and controlled additions of nitrogen to form Ta_2N. Deposition was at a rate of 0.3 nm/s onto the (11$\bar{2}$ 0) surfaces of the single crystal sapphire substrates to a final film thickness of 635 nm. The films were then divided into two groups. One group consisted of as-deposited samples. The second group was heated at 300°C for 100 hours in a vacuum of 1.3×10^{-4} Pa (10^{-6} torr). The thickness of each film was then established by cross-section measurement in a JEOL 840 SEM.

Mechanical Property Testing. The elastic moduli and hardness were determined from a series of indentations on each film employing an indentation test system developed by Nano Instruments, Inc. [12,13] All tests were conducted at a loading rate of 300 μN/s with maximum contact (plastic) displacement ranging from 20 to 800 nm using a Berkovich indenter. Indentation loads and

corresponding displacements were recorded continuously throughout each test. The area for each indentation in the as-sputtered film was determined from an area shape function derived from direct measurements of indentation areas on single crystal aluminum, fused silica, and thin tantalum nitride and aluminum films. The areas for selected indentations in the as-deposited film spanning the full range of test displacements were also measured in a field emission SEM to confirm applicability of the tip shape function. These areas were then used with the slopes from the unloading curves to determine stiffness and elastic modulus following the method of Oliver and Pharr. [13] Hardness was calculated for each test from the maximum load and the area of the indentation.

Fracture Testing. The resistance to interfacial fracture was determined from indentation and nanoscratch tests conducted on two indentation test systems, one developed by Nano Instruments, Inc. and one by IBM. [15,16] The Nano Instruments, Inc. system was configured to control normal loads while the IBM system was configured to control normal displacements. Both systems were configured to control lateral indenter displacements. For the indentation fracture tests, a conical diamond indenter with a nominal 1μm tip radius and a 90° included angle was driven into the films at a loading rate of 500 μN/s (produced from a normal displacement rate of 15 nm/s in the IBM system) until a portion of the film spalled from the substrate. During each test, the normal loads and displacements were continuously monitored. For the nanoscratch tests, a second conical diamond indenter also with a nominal 1μm tip radius and a 90° included angle was simultaneously driven into the films at a loading rate of 500 μN/s and across the films at a lateral displacement rate of 0.5 μm/s until a portion of the film spalled from the substrate. During each test, the normal and tangential loads along with the normal and lateral displacements were continuously monitored.

RESULTS AND DISCUSSION

Materials. Tantalum nitride can exist in several compositionally and structurally distinct forms. [22] TEM showed that the structure of the as-deposited films in this study consisted of a 200-nm-thick amorphous layer near the interface followed by columnar grains of nanometer-size crystallites extending to the surface. (Figure 1) [5,23] Although the film is composed of two distinct structures, scanning auger microscopy showed that the composition was constant with a two-to-one ratio between tantalum and nitrogen through the film thickness. High Resolution TEM showed the interfaces have three-to-four atom layers of amorphous oxide between the sapphire substrate and tantalum nitride film. The presence of this region parallels observations of amorphous oxide layer formation on several different types of oxide substrates following sputter processing. [24] It may also be responsible for the nucleation of amorphous tantalum nitride near the oxide-film interface.

Vacuum annealing of the as-deposited films at 300°C for 100 hours had no observable effect on the microstructure of the films or of the film-substrate interface. The films maintained a 200-nm-thick amorphous layer near the surface followed by columnar grains extending to the surface. Moreover, high resolution TEM showed no discernible effect of annealing on the interface structure. This is consistent with a previous study [25] showing that tantalum and tantalum nitride films neither react with the aluminum oxide substrates nor change lattice structure on exposure to high temperatures in vacuum environments. However, cross-sectional measurements suggest that there were changes on the atomic scale as the average film thickness decreased from 635 nm in the as-deposited films to 530 nm for vacuum annealed films. A decrease in film thickness of this size most likely results from a reduction in the high density of vacancies and micropores created during sputter deposition. [6,7] Atomic force microscopy of the film surfaces also revealed that there was a marked change in surface structure from the random undulations characterizing the as-deposited film surfaces to well-defined parallel striations on the vacuum annealed film surfaces. (Figure 2) This change in structure shows there was significant surface atom movement during elevated temperature exposure.

Several theoretical studies have shown that a planar free surface is unstable in the presence of tensile or compressive stresses leading to ridge, cusp, and groove formation by stress driven surface diffusion. [26-30] The phenomena has been used to explain the ridges observed on $In_{0.25}Ga_{0.75}As$ thin films grown on GaAs(100) surfaces [31] and forwarded as a possible mechanism for surface step and groove formation in Cr_2O_3 scales. [32] The theory also provides an estimate of stresses driving striation formation in the tantalum nitride films of this study. Striation formation occurs when the striation width equals or exceeds the critical wavelength given as follows [30],

$$\lambda_c = \frac{\lambda_p}{2} = \frac{\pi M \gamma}{\sigma^2} \qquad (1)$$

where λ_c is the critical wavelength or striation width for growth, λ_p is the most probable width of striations that form, M is the biaxial modulus of the film, σ is the stress driving striation growth, and γ is the surface tension. Taking γ as 1 J/m^2 and setting the most probable wavelength equal to the average measured striation spacings of 65 and 145 nm crossing the surface, equation (1) gives an effective stress driving the surface perturbations between 4.2 and 6.2 GPa. This value is higher than recent x-ray diffraction measurements of a compressive residual stress of 3.2 GPa in a 400-nm-thick tantalum nitride film deposited under identical conditions [33] but is consistent with observations that residual stress increases with film thickness. [34] Furthermore, this value is typical for compressive residual stresses measured in oxides, diamond, diamond-like carbon, and nitride films. [35-37]

Mechanical Properties. Elastic modulus was determined as a function of indenter depth for both the as-deposited and vacuum annealed films from the indentation load-versus-displacement curves. Figure 3 shows that for the as-deposited films, the measured elastic modulus equals 350 GPa for the first 200 nm of the film and then gradually increases to the substrate value of 400 GPa as contact depth approaches the film-substrate interface. These values were calculated assuming Poisson's ratio is equal to the value of 0.35 for tantalum. The value for Poisson's ratio may be less as often observed for oxides and nitrides, but the effect on elastic modulus is relatively small. There is substantial scatter in measured values within 50 nm of the film surface due primarily to variations in surface topography. This results from the variations in surface height being less than the 300-nm-radius of the Berkovich indenter. There is also an increase in measured elastic modulus with depth due not to the effect of a layered microstructure but to an increasing effect from the substrate. This is shown in recent work where tantalum nitride films on aluminum nitride substrates exist in two forms; one form is a polycrystalline and amorphous layer structure as observed on the sapphire substrates and the other is a single layer polycrystalline structure. [23,38] In both cases the elastic modulus-versus-displacement curves superimpose showing that the microstructure has little effect on properties.

Superimposed on the as-deposited film values in Figure 3 are the measured elastic modulus values for the vacuum annealed film. These values are higher than the as-deposited elastic moduli with an average value of 410 GPa near the film surface. In contrast with the as-deposited film values, the vacuum annealed values decrease with depth to sapphire values near the film-oxide interface. Of particular interest, the near surface elastic moduli scale inversely with film thickness. These values obey a simple rule of mixtures for the effect of void content on modulus. This supports the concept that the increase in elastic modulus and decrease in film thickness is due to a decrease in defect concentration.

The hardness values for both the as-deposited and vacuum annealed films essentially superimpose when measured from the film surface as shown in Figure 4. However, when all values are referenced to the distance from the interface, the near surface vacuum annealed values are slightly higher than the as-deposited values which is consistent with expectations of higher hardness with

higher film density. Regardless of reference location, the near surface hardness values for both films are significantly higher than that of the sapphire substrate. As a result, the as-deposited and vacuum annealed measured hardness values decrease to the value for sapphire at the film-substrate interfaces reflecting an increased contribution from the softer substrate with increasing test depth. The values for hardness and elastic modulus for the tantalum nitride films are significantly greater than pure tantalum values. Nevertheless, the values are similar to the effects of nitrogen, boron, and carbon on elastic modulus and hardness values observed in metals and ceramics. [36,39-41]

Indentation Fracture. During indentation fracture tests, the as-deposited films fracture consistently at loads between 250 and 300 mN producing large circular spalls as shown in Figure 5. The onset of fracture is defined by the rapid excursion of the indenter through the film to the interface at essentially constant load. In all cases, fracture occurred by reverse or double buckle formation during indentation with the material under the indenter pinned to the substrate. There were no observations of buckling or fracture when tests were stopped prior to the displacement excursion. Furthermore, loading beyond the point of rapid excursion did not lead to additional crack growth. These observations clearly show that interfacial crack growth and film fracture occurs rapidly after crack nucleation.

One very interesting observation is that the onset of fracture occurred consistently at plastic depths near 300 nm. This depth corresponds to the thickness of the uniform nanocrystalline portion of the film. Rapid fracture subsequently occurred as the indenter traversed the amorphous region of the film.

Fracture was not observed during any indentation test on vacuum annealed films even at loads of 600 mN and indenter displacements well into the substrate. This strongly suggests that interfacial crack nucleation and propagation in the as-deposited film is driven by high compressive residual stresses. Moreover, these observations indicate that vacuum annealing at least partially relieves residual stresses in these films.

Scratch Fracture. The first nanoscratch tests were run on the IBM indentation test system under displacement control. A subsequent series of scratch tests were run on the as-deposited films on the Nano Indenter II ™ under load control. The results were essentially identical with the tests on both systems revealing a significant difference in fracture behavior between the as-deposited and vacuum annealed films. Failure in the as-deposited film occurred by the formation of large spalls as shown in Figure 6a. There were often a series of spalls occurring sequentially. In all cases, the exposed substrate surfaces were distinctly interfacial in character with no evidence of tantalum nitride within the limits of energy dispersive x-ray diffraction. The fractures occurred consistently at loads near 100 mN and were accompanied by a sharp increase in indenter depth and tangential load as shown in Figure 6b. Beyond the initial point of fracture, the indenter penetrated the sapphire substrate.

Comparison of normal and tangential loads showed that the coefficient of sliding friction on the films was equal to 0.28 and relatively constant throughout most of the test. Just prior to fracture, the coefficient of friction increased to an average value of 0.62 as the indenter grooved into the film and then to an average value of 0.79 as the film fractured and the indenter plunged to the film-substrate interface. Observations suggest that the indenter began grooving into the uniform nanocrystalline portion of the film when the film failed at the film-substrate interface immediately beneath the indenter. Rapid fracture subsequently occurred when the indenter ploughed into the amorphous portion of the film. This sequence of events followed the same process for fracture and dependence on the film microstructure that was observed during indentation fracture tests. The principal difference was that fracture occurred at much lower applied normal loads during the scratch tests than during the indentation fracture tests.

There were several tests on the as-deposited film that produced large asymmetric spalls which wrapped back around the scratch track. In two of these tests the initial spalls triggered uniform width buckles that ran back along much of the scratch track lengths as shown in Figure 7. Formation of the asymmetric spalls followed sample repositioning and are most likely due to a slight misalignment in indenter-to-film surface contact. Nevertheless, these uniform-width buckles provided data to define residual stress levels and strain energy release rates for interfacial fracture.

Failures in the vacuum annealed film occurred at loads near 70 mN which were slightly lower than observed in the as-deposited films. However, the areas of spallation were much smaller in size as shown in Figure 8. Nevertheless, the fracture events were characterized by the same abrupt changes in the load-versus-distance traces. The fracture had the same distinct interfacial appearance as in the as-deposited films and there was no evidence of tantalum nitride remaining on the substrate surface.

One dimensional buckle analysis. The residual stress and the energy for interfacial fracture in the as-deposited film can be determined following the analysis of Hutchinson and Suo [21] for a one-dimensional or straight wall buckle. The analysis is based on the assumption that the film and substrate are elastic isotropic solids, the film is subject to a uniform, equi-biaxial compressive in-plane stress, and the film thickness is much less than the buckle width. The buckle is then modeled as a wide, clamped Euler column of length 2b as shown in Figure 9. For a blister to form in the as-deposited film under these conditions, the compressive residual stress, σ_r, must exceed the stress for delamination, σ_c, as follows [21],

$$\sigma_c = \frac{\pi^2 E}{12(1-\nu^2)}\left(\frac{h}{b}\right)^2 \tag{2}$$

In this expression, E is the elastic modulus of the film, ν is Poisson's ratio, and h, is the film thickness. The residual stress, σ_r, can then be determined from the blister height, δ, and the stress for delamination as follows [21],

$$\sigma_r = \sigma_c\left[\frac{3}{4}\left(\frac{\delta}{h}\right)^2 + 1\right] \tag{3}$$

Using interference microscopy, the buckle height was found to range from 0.3 to 0.5 μm and the buckle half-width from 5.3 to 6.1 μm along the length of the two uniform width blisters. Combining these measurements with an elastic modulus of 350 GPa, a film thickness of 635 nm, and Poisson's ratio of 0.35, equation (3) gives a calculated average compressive residual stress of 5.4 ± 0.7 GPa. This is in good agreement with the stresses calculated to be driving surface atom rearrangement and strongly supports 5.4 GPa as the true value of residual stress in the film. It should be noted that the stresses induced from indenter displacement along the scratch length average less than 100 MPa across the buckle width and were therefore ignored in the analysis.

The strain energy per unit area, G_o, stored in the film and available for fracture is a function of the residual stress as follows [21],

$$G_o = \frac{(1-\nu^2)h\sigma_r^2}{2E} \tag{4}$$

When the film buckles, the separation between the film and substrate loads the edge of the interfacial crack in tension. The tensile stresses drive interfacial crack advance with a release of strain energy given by [21],

$$G = \left[\frac{(1-\nu^2)h}{2E}\right](\sigma_r - \sigma_c)(\sigma_r + 3\sigma_c) \tag{5}$$

This value equals the energy for interfacial fracture, Γ_i, at crack arrest.

In the as-deposited film of this study, the compressive residual stress gives an average strain energy per unit area stored in the film available for fracture of 23.4±5.1 J/m^2. This drives one-dimensional blister formation in the as-deposited film at an average interfacial fracture energy of 17.5±5.5 J/m^2. Although the fracture energy is significantly less than the stored energy, the difference is typical for films where the stress driving film buckling is not much greater than the stress for delamination.

The intrinsic toughness of interfaces is often identified with pure mode I loading. However, the stresses at the crack tip of a buckled film are comprised of mode I and mode II components. For one-dimensional blisters, the phase angle defining the relative contributions of normal mode I and shear mode II loads is given by [21],

$$\tan\psi = \frac{k_{II}}{k_I} = \frac{4\cos\omega + \sqrt{3}\,\xi\sin\omega}{-4\sin\omega + \sqrt{3}\,\xi\cos\omega} \tag{6}$$

In this equation, k_I and k_{II} are the mode I and mode II crack tip stress intensities, ξ equals δ/h, and ω is a dimensionless function of the Dundurs's parameters, α and β, which describes the elastic mismatch between the film and the substrate. As there is little elastic mismatch between the films and substrates in this study, ω reduces to 52.1°. [21] The corresponding phase angle of loading for the one-dimensional buckle in the as-deposited film is equal to -53.1±3.0°. This angle shows there is a significant amount of both mode I and mode II loading.

Indentation Fracture Analysis. The indentation fracture tests in the as-deposited film trigger axisymmetric buckling and subsequent fracture from which the fracture energy can also be obtained. In all these fractures, the center is constrained giving rise to a reverse or double buckle configuration as shown schematically in Figure 10. For small buckling deflections, Marshall and Evans [19] and Evans and Hutchinson [20] derived an asymptotic solution for strain energy release rate by modeling the axisymmetric blister as a completely clamped circular plate with a radius much greater than the film thickness and subject to an equi-biaxial compressive stress. In the as-deposited films of this study, the compressive stress is comprised of the stress due to indentation and the residual stress. Assuming a rigid substrate and that all material plastically displaced during indentation goes into the film, the stress due to indentation is [19,20],

$$\sigma_v = \frac{EV}{2\pi(1-\nu)a^2h} \tag{7}$$

where σ_v is the radial stress in the plane of the film due to indentation, V is the plastic volume of material displaced into the film, a is the crack radius, h is the film thickness, E is the elastic modulus of the film, and ν is Poisson's ratio. When added to the residual stress, the total compressive stress in the film must exceed the stress for delamination. The stress for delamination is given by [19,20],

$$\sigma_c^* = \frac{kE}{12(1-\nu^2)}\left(\frac{h}{a}\right)^2 \tag{8}$$

where the constant k equals 42.67 for a circular clamped plate with a constrained center point and 14.68 when the center is unconstrained.

When the film buckles during indentation, the tensile stresses at the edge of the circular crack drive crack advance. Marshall and Evans [19] have derived the strain energy release rate for a circular buckle due to residual and indentation stresses as follows, [19,33]

$$G = \frac{(1-\nu)h\sigma_r^2}{E} c \left[\left(1 - \frac{\sigma_c^2}{\sigma_r^2} \right) + \left(\frac{\sigma_v^2}{\sigma_r^2} \right) \left(\frac{2\sigma_c}{\sigma_v} + \frac{(1+\nu)}{2c} - 1 \right) \right] \tag{9}$$

where $c=[1+0.902(1-\nu)]^{-1}$ from Hutchinson and Suo [21]. The first term gives the contribution from residual stress and the second term gives the contribution from indentation. In the absence of indentation stresses, Hutchinson and Suo [21] have shown that equation (9) is valid only for ratios of σ_r/σ_c up to three for the single buckle configuration. Beyond this value, more accurate solutions using the finite difference method have been derived. However, these solutions are valid for only residual stress induced fracture and then only for the single buckle configuration.

During the indentation fracture tests, the displacement-induced stresses act with the compressive residual stresses to nucleate fracture and drive interfacial crack propagation. Observations of the load-deflection curves and of the film surfaces reveal that fracture begins when the indenter has partially penetrated the film thickness. Once the interface crack has nucleated, the indenter plunges to the film-substrate interface. However, it cannot be determined if crack advance is driven to completion from the stored energy at the onset of crack nucleation or if additional crack growth occurs as the indenter drives to the film-substrate interface. In either case, the additional stresses and strain energy from indentation are relatively small in comparison to residual stress effects. As atomic force microscopy has shown, fully two fifths of the displaced material is thrust up around the indenter and not into the film. [42] Most likely much of the material under the indenter at the onset of fracture is from the amorphous portion of the film and remains under the indenter as it drives to the film-substrate interface. With the observation that three fifths of the displaced material is compressed into the film and the assumption that fracture goes to completion, the average strain energy release rate value is 9.8 ± 5.0 J/m^2 at the first indication of fracture. This provides a lower limit for the fracture energy. At the end of the fracture excursion, the average strain energy release rate is 13.2 ± 4.8 J/m^2. This provides an upper limit and more appropriate value for interfacial fracture energy as it is determined assuming that the effects of including all material under the indenter in the analysis offset the lower strain energy obtained when films spall prior to crack arrest. In either case, the values are well within the region of validity for equation (9).

Of particular note, no interfacial fracture could be induced in the vacuum annealed films during repeated indentation tests. The tests were conducted at loads almost three times those needed for as-deposited film fracture and at plastic depths well beyond the film-substrate interface. These results suggest that vacuum annealing reduced or eliminated the compressive residual stresses in the films. It also reveals that vacuum annealing greatly reduces susceptibility to fracture from normal loads.

Since solutions for the phase angle of loading have not been determined for reverse or double buckling failures, an approximation for the phase angles can be obtained by using the circular blister solutions of Hutchinson and Suo. [21] Beginning with the calculated strain energy release rate from equation (9), the effective loading parameter, σ_c^*/σ_r, is back-calculated as follows, [21]

$$\frac{\sigma_c^*}{\sigma_r} = \left[1 - \frac{G}{G_o^* c_1}\right]^{1/2} \tag{10}$$

with

$$G_o^* = \frac{(1-\nu)h\sigma_r^2}{E} \tag{11}$$

and is used to determine buckling amplitude, ξ.

$$\xi = \frac{\delta}{h} = \left[\frac{1}{c_1}\left(\frac{\sigma_r}{\sigma_c^*} - 1\right)\right]^{1/2} \tag{12}$$

The corresponding phase angle of loading is then given by,

$$\tan\psi = \frac{\cos\omega + 0.2486(1+\nu)\,\xi\sin\omega}{-\sin\omega + 0.2486(1+\nu)\,\xi\cos\omega} \tag{13}$$

where ω=52.1° and c_1=0.2473(1+ν)+0.2231(1-ν^2). The corresponding phase angle of loading is -56.5±2.9°. As for the one-dimensional blister, the phase angle shows that there is a significant effect of mode II loading on measured fracture energy.

Scratch Test Fracture Analysis. There have been no rigorous determinations of interfacial fracture energies from scratch test results. However, there have been approximations based on the energy stored from elastic stress distributions. [14,17,37,43] We can use the elastic approximation of Venkataraman et al. [14,17] to estimate the energy stored in the film and the circular buckle analysis of Marshall and Evans [19] and Hutchinson and Suo [21] to estimate the strain energy release rates for fracture. Following the elastic approximation of Venkataraman et al., [14,17] the elastic strain energy stored in the film from the scratch test elastic stress distributions is given by,

$$G_o = \sum\left(\frac{(1-\nu^2)\bar{\tau}_{ij}^2 h}{2\mu} + \frac{(1-\nu^2)\bar{\sigma}_{ij}^2 h}{2E}\right) \tag{14}$$

In this expression, G_o is the stored elastic strain energy available for fracture, and $\bar{\tau}_{ij}$ and $\bar{\sigma}_{ij}$ are the average elastic shear and normal stresses in the delaminated film. It should be noted that in the original derivation, the energy was taken as twice the value given in equation (14) based on the assumption that an equal amount of energy was also released into the substrate on delamination. In this study, the analysis of Venkataraman et al. [14,17] has been modified so that only the energy in the film is assumed to drive delamination to be consistent with other studies. In addition, the contributions for all stress components have been determined explicitly from the critical normal and tangential loads at failure, the area and length of the debonded region, and the scratch width at the point of delamination. The total strain energy stored in the as-deposited film above the delamination available for fracture is determined by summing residual stress and scratch test contributions as follows,

$$G_o = \frac{(1-\nu^2)\sigma_r^2 h}{2E} + \sum\left(\frac{(1-\nu^2)\bar{\tau}_{ij}^2 h}{2\mu} + \frac{(1-\nu^2)\bar{\sigma}_{ij}^2 h}{2E}\right) \tag{15}$$

The energy stored in the film from applied forces has also been calculated for the case where the indenter has essentially penetrated the film before fracture as in the tests on the vacuum annealed sample. In this case, the average stresses were determined following the method employed by Vankataraman et al. [14,17] using the distributions given by Timoshenko and Goodier [44] for a force acting along a line in a plane.

Based on the observation that most spalls are circular and symmetric about the scratch track, the strain energy release rates can be estimated using a circular blister analysis. [19-21] (Figure 11) In this approach, the delamination stress is determined from measured spall radii using equation (8) for an unconstrained center point and the following equation for strain energy release rate, [19-21]

$$G = \frac{(1-\nu)h\sigma^2}{E} c\left[\left(1-\frac{\sigma_c^*}{\sigma}\right)^2\right] \tag{16}$$

where $c=[1+0.902(1-\nu)]^{-1}$. [21] The strain energy release rates for the as-deposited film were then calculated using equation (16) with the effective stress, σ, driving fracture back-calculated from the total stored energy and the first term in equation (15). The phase angles of loading were determined from equations (10) through (13), and the numerical solutions presented by Hutchinson and Suo [21] for the cases where σ_c/σ_r ratios were greater than three.

The results are given in Table I where A is the area of spallation, P_{cr} and L_{cr} are the critical normal and tangential loads for fracture respectively, $G_{applied}$ and G_{total} are the applied and total stored strain energies at fracture respectively, Γ_{I-II} is the measured fracture energy, ψ is the phase angle of loading , and Γ_I is the projected mode I fracture energy. As this table shows, the loads at fracture in the as-deposited film were virtually identical for tests producing symmetric and asymmetric spalls. However, the spall widths, lengths, and orientations differed significantly. This led to stored energies from the applied stresses a factor of two lower for tests producing asymmetric spalls. These values were small in comparison to the total stored energy for fracture which averaged 23.7±5.2 J/m^2 for tests producing symmetric spalls and 23.5±5.2 J/m^2 for tests producing asymmetric spalls. The standard deviation includes contributions from the residual stress and scratch test measurements. It should be noted that the scratch test stress distributions had almost no effect on the stored energies in either case. The corresponding strain energy release rates at fracture averaged 15.5±6.4 J/m^2 for tests producing symmetric spalls and 20.0±4.4 J/m^2 for tests producing asymmetric spalls. The phase angles of loading are -60.1° and -64.4° respectively. Not surprisingly, the fracture energies and phase angles of loading are in reasonably good agreement with one-dimensional blister and indentation fracture results.

The scratch tests also induced fracture in the vacuum annealed films at slightly lower loads than required for fracture in the as-deposited films. Fracture was still characterized by an abrupt change in the load-versus-displacement curves but was not followed by sudden large scale spallation characteristically driven by high residual stresses. In the absence of high compressive residual stresses, the scratch test produces strong asymmetric stress gradients which serve to limit crack advance. [14,16,17] Indeed, the areas of spallation were much smaller with little advance away from the scratch track trace. As a result, the applied stress contributes a significant amount of stored energy to the film as shown in Table II where the stored energy from the applied stress just prior to the indenter plunge into the film averages 28.5±13.1 J/m^2.

In contrast to the as-deposited films where buckling and spallation occur when the indenter has partially penetrated the film, spallation in the vacuum annealed film appears to occur when the indenter has fully penetrated the film. Under these conditions, the elastic stored energy is estimated from forces acting along a line through the film perpendicular to the film surface. However, this

film does not spall catastrophically and a circular blister analysis cannot be used to determine the strain energy release rate at fracture nor the mode I contribution to fracture. Nevertheless, comparison with stored energies at fracture in the as-deposited film provides insight into the fracture process and mechanics of adhesion. There is no change in microstructure along the interface nor any discernible change in composition between the as-deposited and vacuum annealed films. Without a change in structure or composition, the fracture energies of these films would be similar if there is no additional contribution from bond strength. Under this assumption, any remaining residual stress in the vacuum annealed film is less than 4.5 GPa. And based on the much smaller areas of spallation in comparison with as-deposited film failure, any remaining residual stress is much less than 4.5 GPa. Clearly, the results show that vacuum annealing relieved a substantial portion of the residual stress.

Solutions have not been derived for strain energy release rates in films with asymmetric stress distributions or strong stress gradients as observed in the vacuum annealed film of this study. Nevertheless, the scratch test results suggest that the stresses driving fracture in this film are only slightly greater than the stress for delamination. As a consequence the strain energy release rate is most likely a fraction of the total stored energy similar in magnitude to that observed in the as-deposited film.

Mode I Fracture Energies and Adhesion. Treating the fractures in this study as inherently mode I failures [45], the mode I contributions to fracture were estimated for all tests in this study as follows, [21,46]

$$\Gamma=\Gamma_I (1+\tan^2\psi) \qquad (17)$$

These values are given in Tables I and II, and shown in Figure 12 and 13 where they essentially divide into two different behaviors based on the fracture process. The fracture energy values for one-dimensional blister formation where failure occurred exclusively along the film-substrate interface are almost two times higher than the fracture energies for indentation and scratch fractures where the films fractured and spalled from the surface. The mode I one-dimensional fracture energies correspond to interfacial failure while the mode I indentation and scratch energies may more appropriately reflect conditions for film fracture. Nevertheless, all fracture energies are significantly higher than van der Waals forces and somewhat higher than forces for chemical bonding. Residual stress effects have been accounted for, the elastic contributions are small, and atomic peening effects from high energy bombardment during deposition would be included in the residual stresses. Effects not accounted for in the analysis and not dealt with experimentally are interface roughness on the atomic scale and plastic energy dissipation. Surface roughness can have a substantial effect on macroscopic fractures. [47] It is present along the film-substrate interface on the atomic scale resulting from the RF backsputter cleaning procedure or during the initial stages of sputter deposition. A potentially larger effect on fracture energy can come from plastic energy dissipation during ductile grooving just prior to film fracture. In either case, the ability to test small volumes of material has directed attention to atomic scale processes controlling deformation and fracture of thin films.

CONCLUSIONS

In this study, indentation fracture and continuous nanoscratch testing were used to determine the effects of compressive residual stresses on the fracture of as-deposited and vacuum annealed thin tantalum nitride films on sapphire substrates. The only discernible effect of vacuum annealing was a surface rearrangement of atoms into parallel arrays of striations revealing the existence of a high intrinsic compressive residual stress in the as-deposited films. This stress had a strong effect on fracture as shown by the as-deposited films which fractured readily during indentation and scratch tests forming large circular spalls and uniform-width buckles. The vacuum annealed films on-the-

other-hand exhibited a much lower susceptibility to fracture during scratch tests and no susceptibility to fracture during indentation. Application of mechanics-based models showed that the uniform-width buckles formed under a compressive residual stress of 5.4 GPa. In addition, the measured strain energy release rate for interfacial fracture was 17.5±5.5 J/m^2. This value is a product of mixed mode loading with a mode I contribution of 6.2 J/m^2 at crack arrest. The strain energy release rates for indentation fracture and scratch tests ranged from 13.2±4.8 to 20.0±4.4 J/m^2 in good agreement with the one-dimensional buckle result. The corresponding mode I contribution ranged from 3.4±0.9 to 3.8±0.9 J/m^2 which is a factor of two lower than in the one-dimension buckle case. The mode I one-dimensional fracture energies correspond to interfacial failure while the mode I indentation and scratch energies may more appropriately reflect conditions for film fracture. In all cases the values are significantly higher than van der Waals forces and somewhat higher than forces for chemical bonding. These relatively high mode I fracture energies may result from the effects of interface roughness on the fracture process or plastic energy dissipation during ductile grooving just prior to film fracture.

REFERENCES

1. K. L. Mittal, *Electrocomponent Science and Technology* **3**, 21 (1976).
2. A. G. Evans and M. Ruhle, *MRS Bulletin*, **XV** (10), 46 (1990).
3. K. P. Tremble and M. Ruhle, in *Metal-Ceramic Interfaces*. p. 144, Pergammon Press, Oxford (1990).
4. J. R. Adams and D. K. Kramer, *Surface Science* **56**, 482 (1976).
5. C. L. Au, W. A. Anderson, D. A. Schmitz, J. C. Flassayer, and F. M. Collins, *J. Mater. Res.* **5**, 1224 (1990).
6. R. C. Sun, T. C. Tisone, P. D. Cruzan, *J. Applied Phys.* **46**, 112 (1975).
7. E. Klokholm, *J. Vac. Sci. Technol.* **8** , 148 (1971).
8. D. P. Brady, F. N. Fuss, and D. Gerstenberg, *Thin Solid Films* **66**, 287 (1980).
9. H. C. Cao and A. G. Evans, *Mech. of Materials* **7**, 295 (1989).
10. P. G. Charalambides, J. Lund, A. G. Evans, and R. M. McMeeking, *J. Applied Mechanics* **56**, 77 (1989).
11. Z. Suo and J. W. Hutchinson, *Mater. Sci. Engng.* **A107**, 135 (1989).
12. M. F. Doerner and W. D. Nix, *J. Mater. Res.* **1**, 601 (1986).
13. W. C. Oliver and G. M. Pharr, *J. Mater. Res.* **7**, 1564 (1992).
14. S. K. Venkataraman, D. L. Kohlstedt, and W. W. Gerberich, *J. Mater. Res.* **8**, 685 (1993).
15. T. W. Wu, C. Hwang, J. Lo, and P. S. Alexopoulos, *Thin Solid Films* **166**, 299 (1988).
16. T. W. Wu, *J. Mater. Res.* **6**, 407, (1991).
17. S. K. Venkataraman, D. L. Kohstedt, and W. W. Gerberich, *J. Mater. Res.* **7**, 1126 (1992).
18. S. K. Venkataraman, D. L. Kohlstedt, and W. W. Gerberich, *Thin Solid Films* **223**, 269 (1993).
19. D. B. Marshall and A. G. Evans, *J. Appl. Phys.* **56**, 2632 (1984).
20. A. G. Evans and J. W. Hutchinson, *Int. J. Solids Structures* **20**, 455 (1984).
21. J. W. Hutchinson and Z. Suo, *Advances in Applied Mechanics*, **29**, p.64, Academic Press, Inc., New York (1992).
22. T. B. Massalski, *Binary Alloy Phase Diagrams*, 2nd ed., ASM International, Metals Park (1990).
23. J. E. Angelo, N. R. Moody, S. K. Venkataraman, and W. W. Gerberich, *Mater. Res. Soc. Proc.* **357**, 195 (1995).
24. B. Baretzky, Private communication, Max-Planck Institut fur Metallforschung, Stuttgart, Germany (1996).
25. X.-A. Zhao, E. Kolawa, and M.-A. Nicolet, *J. Vac. Sci. Technol. A* **4**, 3139 (1986).
26. M. A. Grinfel'd, *Sov. Phys. Dokl.* **31**, 831 (1988).
27. C.-H. Chiu and H. Gao, *Mater. Res. Soc. Symp. Proc.* **356**, 33 (1995).
28. W. H. Yang and D. J. Srolovitz, *Phys. Rev. Ltrs.* **71**, 1593 (1993).
29. F. Jonsdottir, *Mater. Res. Soc. Symp. Proc.* **356**, 45 (1995).

30. J. Grilhe, *Acta Metall. Mater.* **41**, 909 (1993).
31. S. E. Harvey, J. E. Angelo, and W. W. Gerberich, *Mater. Res. Soc. Symp. Proc.* **308**, 433 (1995).
32. Y. Zhang, W. W. Gerberich, and D. A. Shores, *J. Mater. Res.* **12**, 697 (1997).
33. D.F. Bahr, J.W. Hoehn, N.R. Moody, and W.W. Gerberich, *Acta Materialia*, (in press).
34. J. A. Thornton and D. W. Hoffman, *J. Vac. Soc. Technol.* **14**, 164 (1977).
35. D. F. Cardinale, D. G. Howitt, K. F. McCarty, D. L. Medlin, P. B. Mirkarimi, and N. R. Moody, *Diamond and Related Materials* **5**, 1295 (1996).
36. K. Messaoudi, A. M. Huntz, B. Lesage, C. Haut, and J. L. Lebrun, and V. Ji, *Corrosion-Deformation Interactions*, The Institute of Metals, London (1997) in press.
37. P. J. Burnett and D. S. Rickerby, *Thin Solid Films* **157**, 233 (1988).
38. N. R. Moody, D. Medlin, and D. P. Norwood, *Mater. Res. Soc. Symp. Proc.* **436**, 97 (1997).
39. M. Wang, K. Schmidt, K. Reichelt, H.. Dimigen, and H. Hubsch, *J. Mater. Res.*, **7**, 667 (1992).
40. M. E. O'Hern, R. H. Parrish, and W. C. Oliver, *Thin Solid Films* **181**, 357 (1989).
41. P. K. Philip, *Wear* **47**, 45 (1978).
42. S. K. Venkataraman, J. C. Nelson, N. R. Moody, D. L. Kohlstedt, and W. W. Gerberich, *Mater. Res. Soc. Symp. Proc.* **343**, 597 (1994).
43. S. J. Bull, D. S. Rickerby, A. Matthews, A, Leyland, A. R. Pace, and J. Valli, *Surface and Coatings Technol.* **36**, 503 (1988).
44. S. Timoshenko and J. N. Goodier, Theory of Elasticity, 3rd ed., p. 127, McGraw-Hill Book Company, New York (1970).
45. A. G. Evans, M. Ruhle, B. J. Dalgleish, and P. G. Charalambides, in *Metal-Ceramic Interfaces*. p. 345, Pergammon Press, Oxford (1990).
46. M. D. Thouless, J. W. Hutchinson, and E. G. Liniger, *Acta Metall. Mater.* **40**, 2639 (1992).
47. A. G. Evans and J. W. Hutchinson, *Acta Metall.*, **37**, 909 (1989).

Table I. Scratch test data and fracture energies from tests on as-deposited thin tantalum nitride films.

A (μm^2)	P_{cr} (mN)	L_{cr} (mN)	$G_{applied}$ (J/m^2)	G_{total} (J/m^2)	Γ_{I-II} (J/m^2)	ψ (degrees)	Γ_I (J/m^2)
Symmetric Fracture							
210±62	98±9	60±6	0.3±0.2	23.7±5.2	15.5±6.4	-60.1±7.5	3.4±0.9
Asymmetric Fracture							
393±137	107±22	69±18	0.1±0.2	23.5±5.2	20.0±4.4	-64.4±7.5	3.6±1.6

Table II. Comparison of scratch test data and fracture energies from tests on as-deposited and vacuum-annealed thin tantalum nitride films.

A (μm^2)	P_{cr} (mN)	L_{cr} (mN)	$G_{applied}$ (J/m^2)	$G_{residual}$ (J/m^2)	G_{total} (J/m^2)	$\sigma_{residual}$ (GPa)
As-Deposited						
210±62	98±9	60±6	0.3±0.2	23.4±5.1	23.7±5.1	-5.4±0.7
VA 300°C/100h						
10±4	70±6	58±8	28.5±13.1	--	28.5±13.1	--

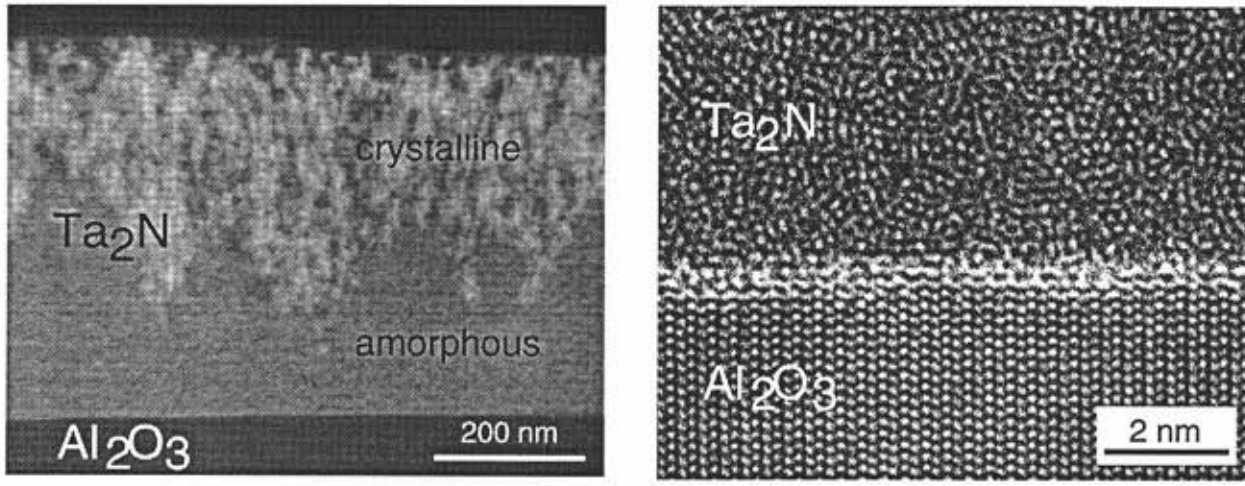

(a) (b)

Figure 1. The microstructure of as-deposited films (a) consists of a 200-nm-thick amorphous region near the interface followed by columnar grains extending to the film surface. The interface between the film and substrate (b) is characterized by a three-to-four atom-layer transition from an amorphous to a crystalline structure.

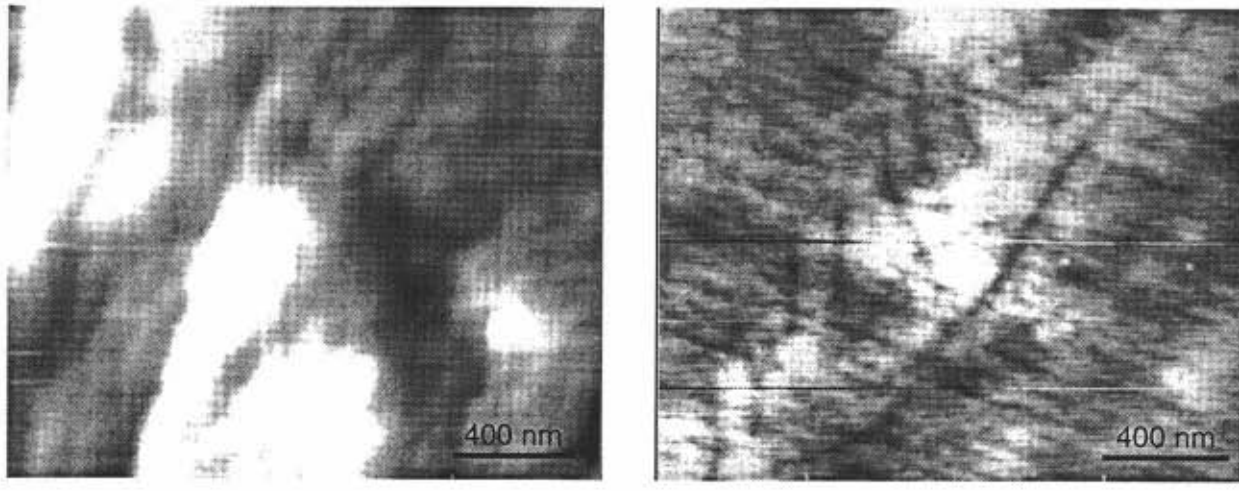

(a) (b)

Figure 2. Atomic force microscopy shows that the (a) as-deposited film surface exhibits small random variations in topology. (b) The vacuum-annealed film surface has rearranged into two parallel arrays of uniformly spaced striations.

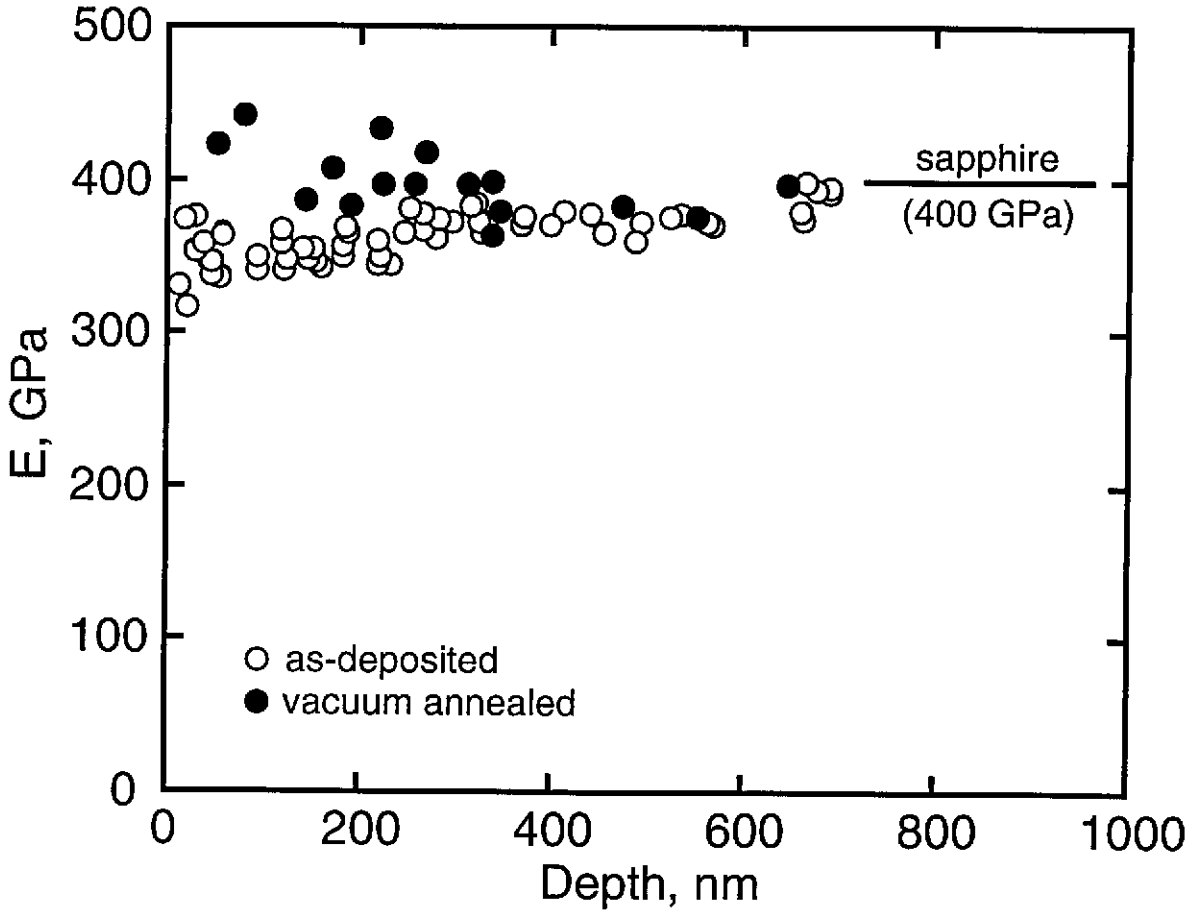

Figure 3. The elastic modulus measured in the as-deposited film increases from 350 GPa near the film surface to the sapphire substrate value of 400 GPa at the film-substrate interface. The vacuum annealed modulus is slightly higher near the film surface reflecting the effect of increased film density.

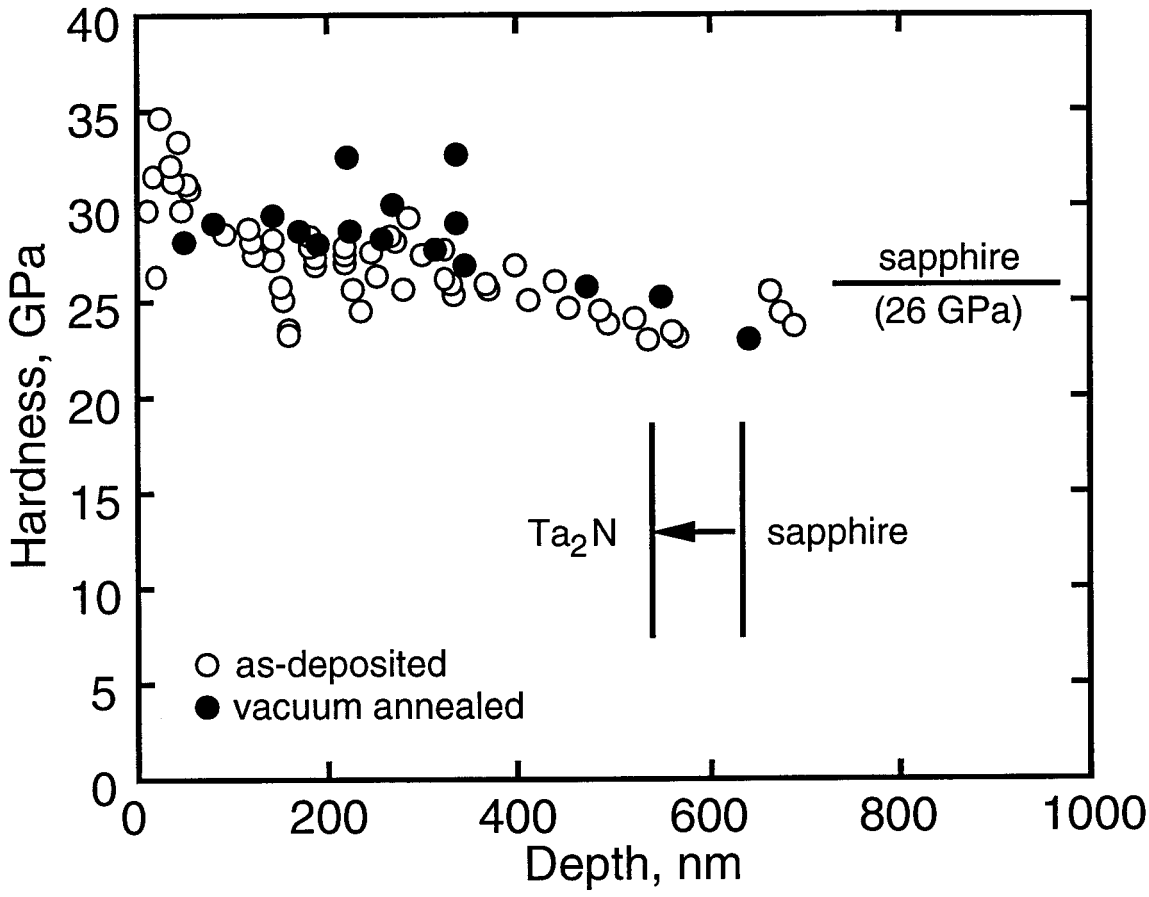

Figure 4. The hardness values for as-deposited and vacuum-annealed films superimpose when measured from the film surface. These values range from 30 to 35 GPa near the film surface to near 25 GPa at the film-substrate interface.

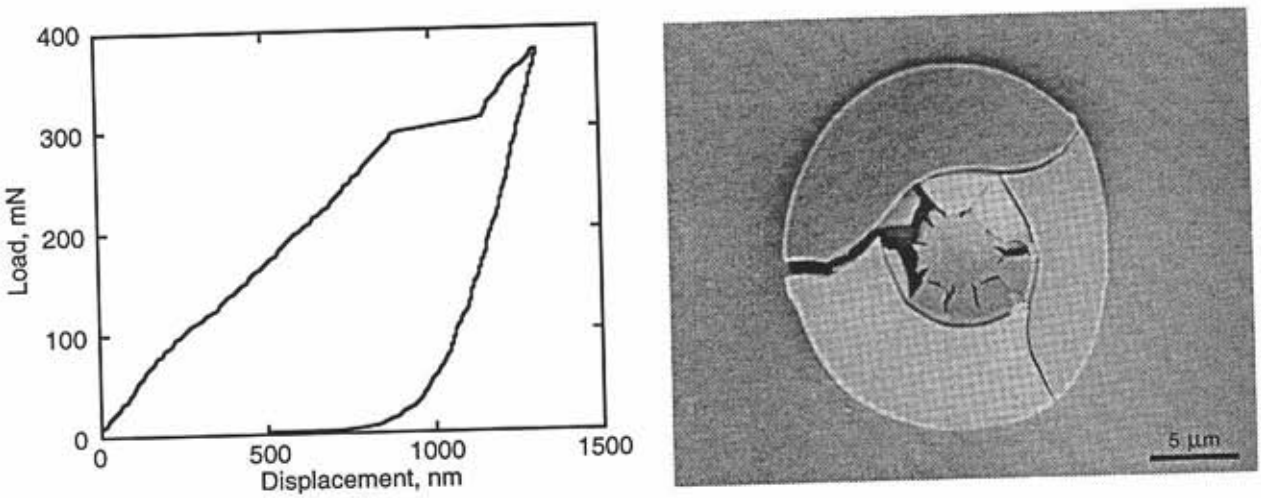

(a) (b)

Figure 5. (a) Indentation fracture of as-deposited film occurred consistently at loads between 250 and 300 mN producing (b) large circular spalls . In all fracture tests, the center point was constrained giving rise to a reverse or double buckle configuration.

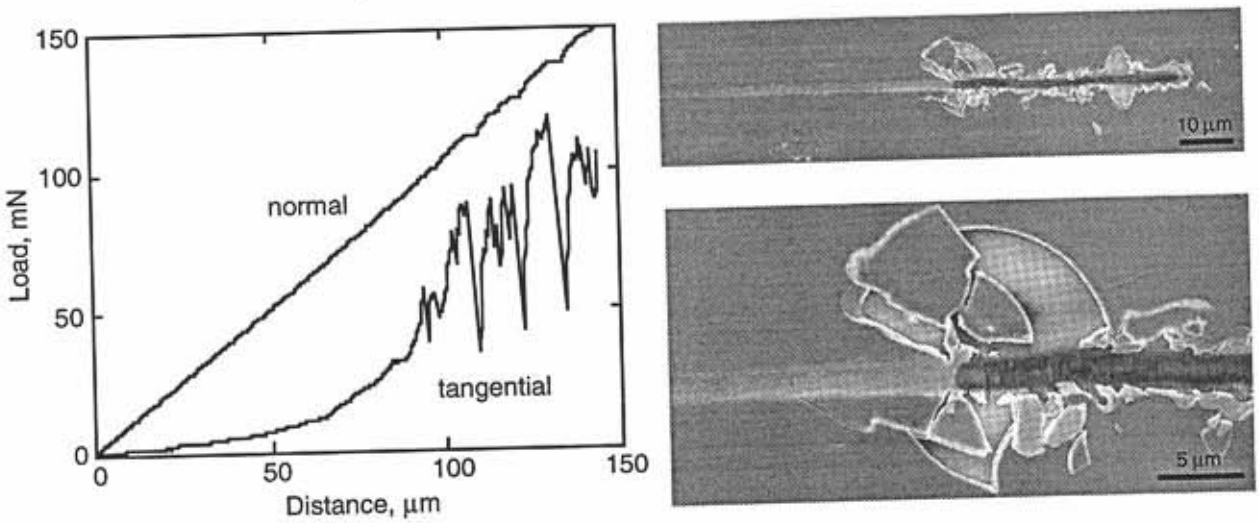

(a) (b)

Figure 6. Scratch test fractures in the as-deposited film (a) occurred consistently near 100 mN and were characterized by an abrupt increase in tangential load. (b) The fractures propagated along the film-substrate interfaces producing well-defined spalls ahead of the indenter.

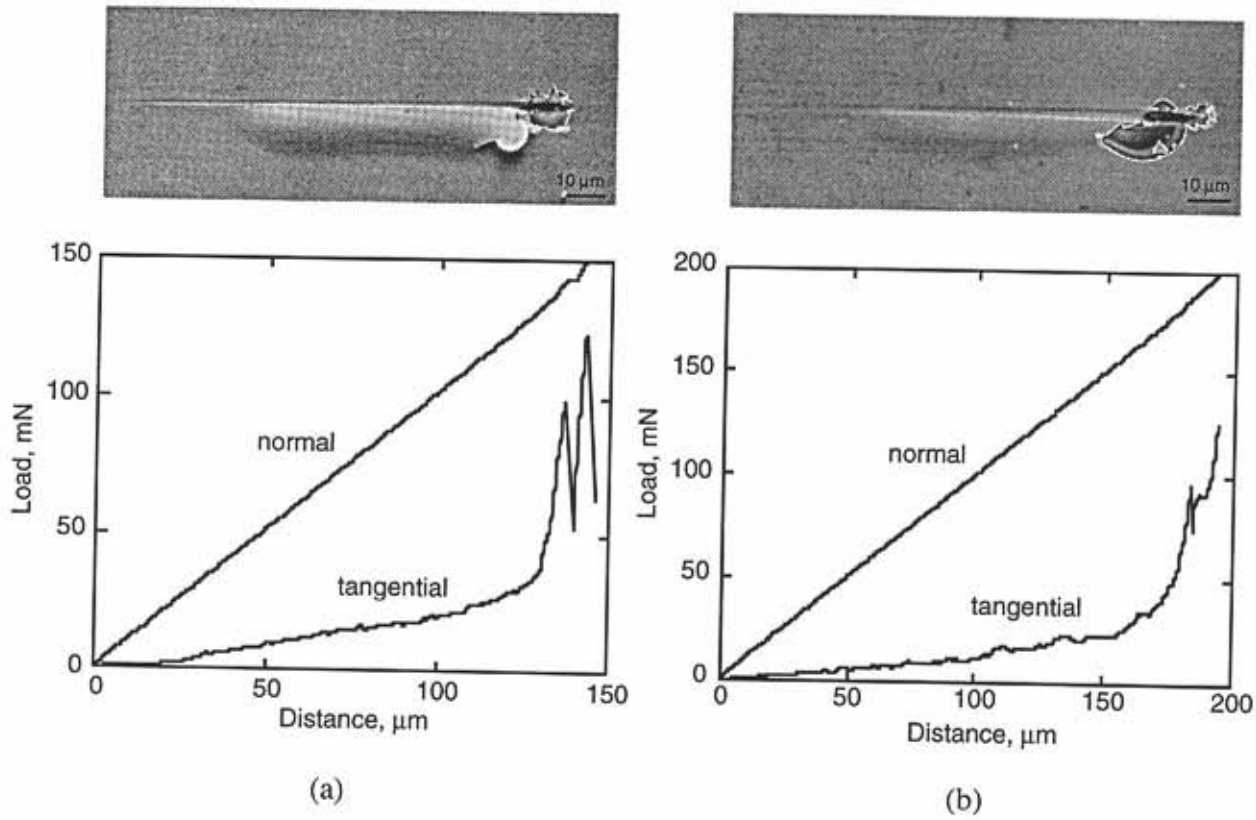

Figure 7. Two scratches triggered uniform width buckles that propagated back along much of the scratch track length.

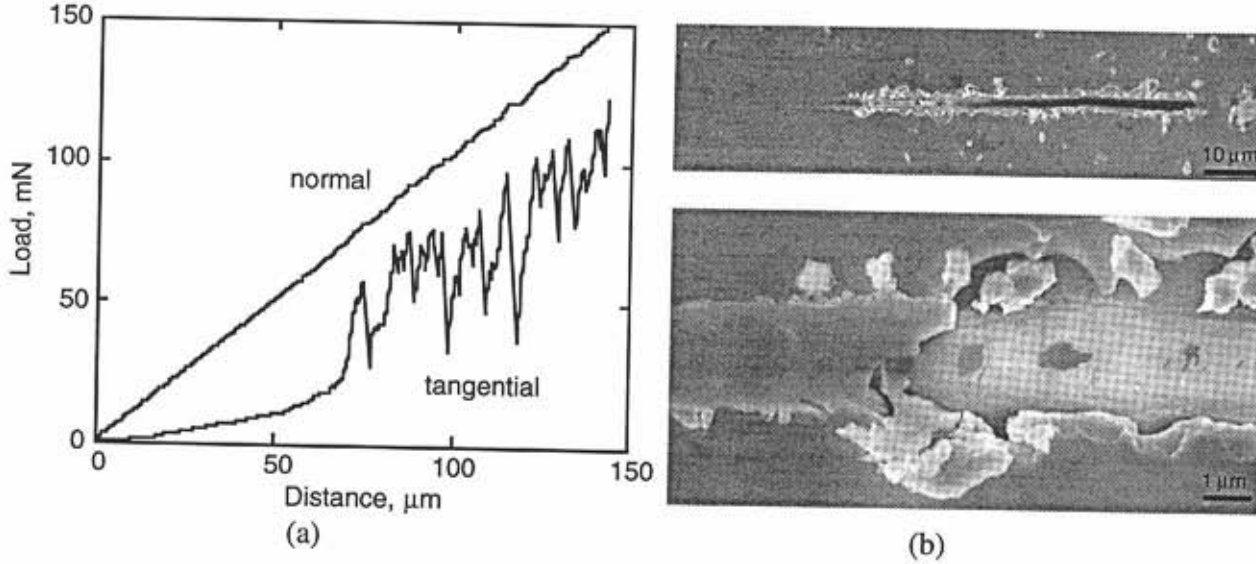

Figure 8. Scratch test fractures in the vacuum-annealed film (a) were characterized by the same abrupt change in tangential loads that was observed in the as-deposited film. (b) However, the spalls were much smaller.

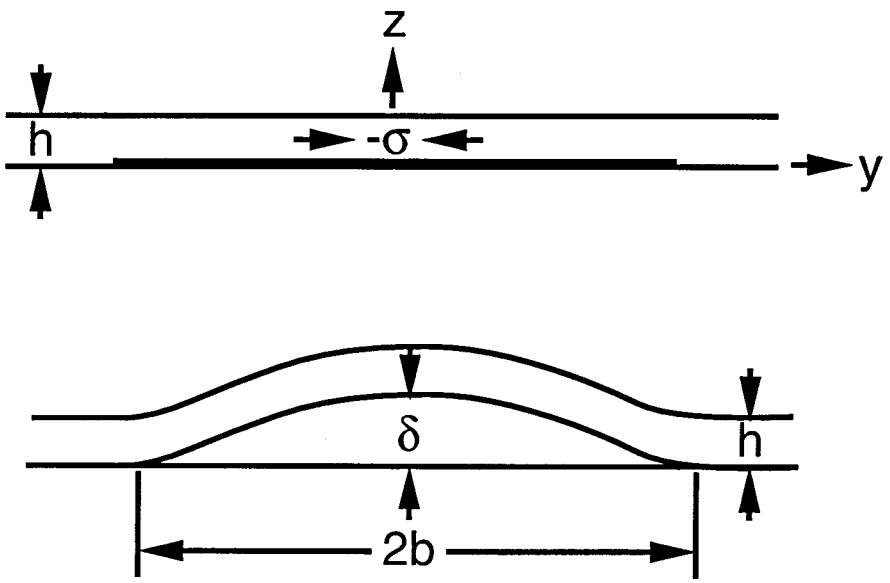

Figure 9. The uniform width buckle in a cross-section schematic shows the relationship between buckle width, buckle height and film thickness.

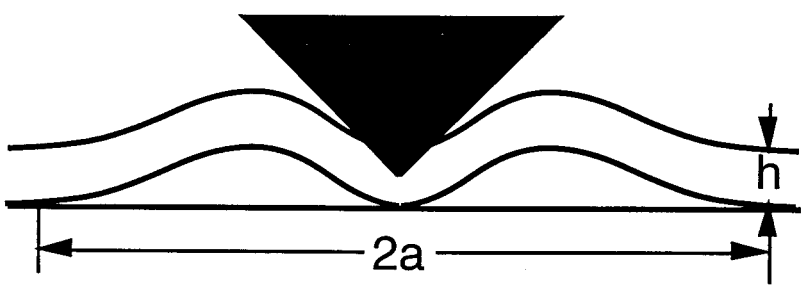

Figure 10. A cross-section schematic shows the axisymmetric character of the reverse or double buckle configuration produced by indentation testing.

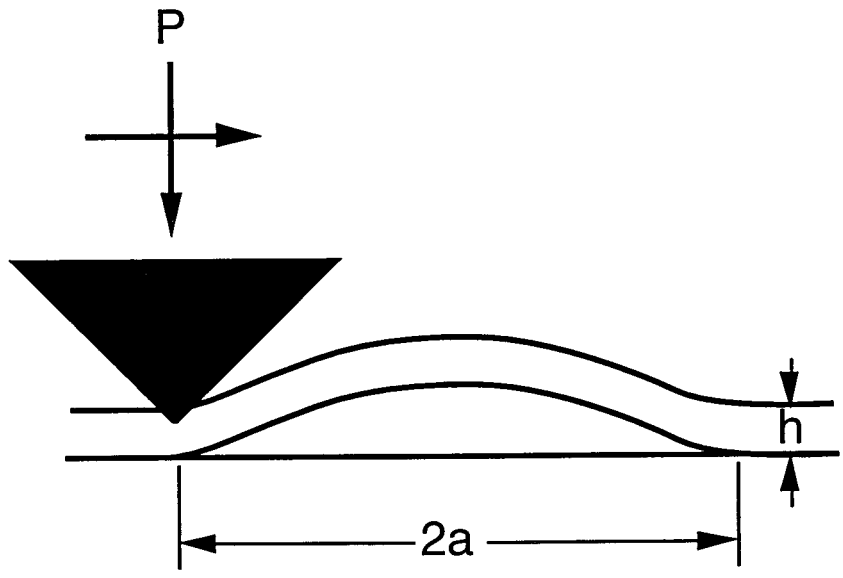

Figure 11. The scratch test fracture of the as-deposited film can be modeled using the circular buckle analysis where the scratch test stresses trigger delamination while the residual stresses drive crack propoagation and film fracture.

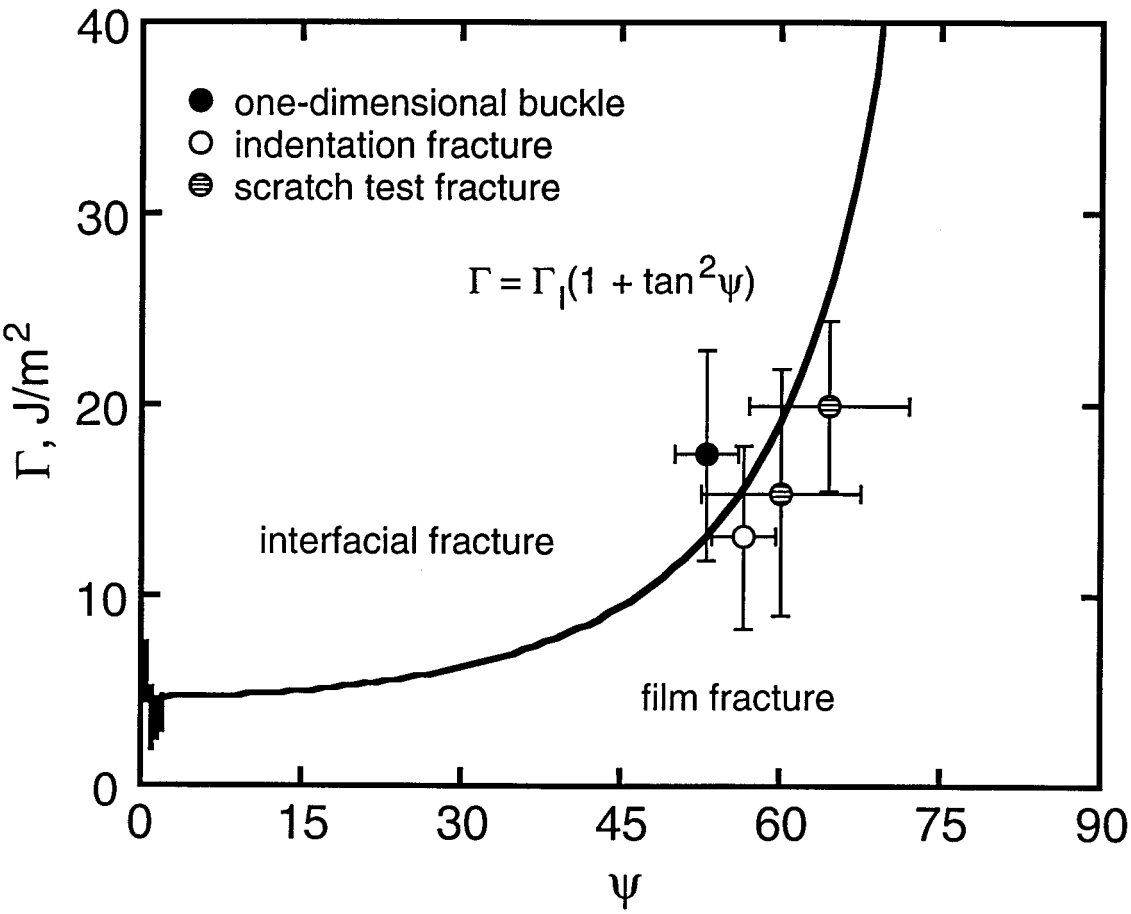

Figure 12. The uniform width buckle, indentation fracture, and scratch test fracture energies group according to fracture process.

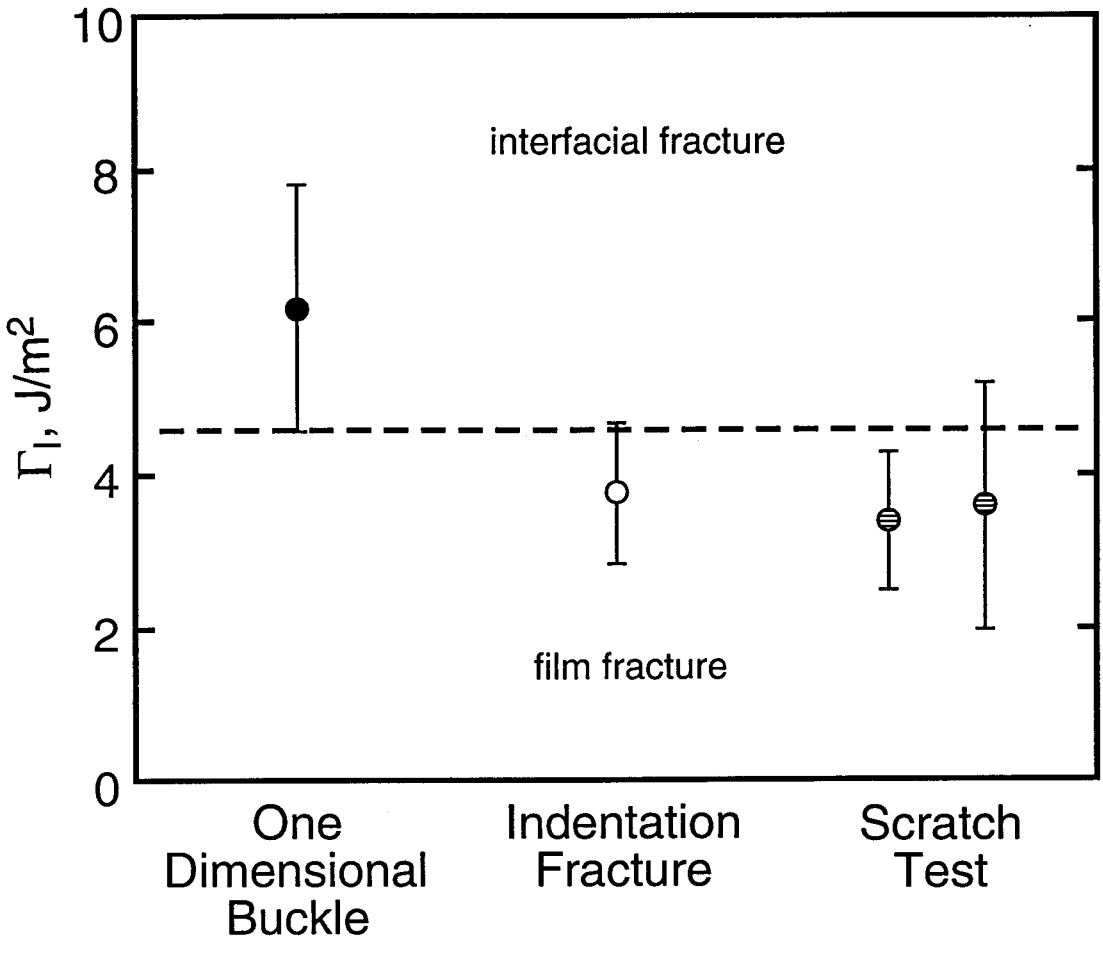

Figure 13. Projected mode I fracture energies clearly group according to fracture process. The film fracture values are on the order of chemical bonding energies while the interfacial fracture energy is a factor of two higher.

DISTRIBUTION:

1 Aeronautical and Maritime Research Laboratory
DSTO
Materials Science and Engineering
Attn: Dr. Stan Lynch
P. O. Box 4331
Melbourne, Victoria 3001
Australia

1 Allied-Signal FM&T
Kansas City Division
Attn: James Sim
P. O. Box 419159, MD40
Kansas City, MO 64141-6159

1 Allied-Signal FM&T
Kansas City Division
Attn: Larry Zawiki
P. O. Box 419159, MG39
Kansas City, MO 64141-6159

5 Applied Materials
Attn: Shankar Venkataraman
3330 Scott Blvd.
MS 0688
Santa Clara, CA 95054

1 Aristotle University of Thessaloniki
Laboratory of Mechanics Polytechnic School
Attn: Elias C. Aifantis
Thessaloniki 54006
Greece

1 Aristotle University of Thessaloniki
Solid State Section
Attn: Prof. Stergios Logothetidis
Thessaloniki 54006
Greece

1 Battelle Pacific Northwest
Attn: Russell H. Jones
P. O. Box 999
MSIN P8-15
Richland, WA 99352

1 Brown University
Division of Engineering Box D
Attn: Clyde L. Briant
182 Hope Street
Providence, RI 02912

1 Brown University
Division of Engineering Box D
Attn: Allan Needleman
182 Hope Street
Providence, RI 02912

1 California Institute of Technology
Graduate Aeronautical Laboratories
Attn: Michael Ortiz
Mail Code 105-50
1201 E. California Blvd
Pasadena, CA 1125

1 Crystallume
Attn: Michael D. Drory
3506 Bassett Street
Santa Clara, CA 95054

1 General Electric Corporate R&D Center
Attn: Don M. Lipkin
One Research Circle
Niskayuna, NY 12309

1 Harvard University
DEAS
Attn: Prof. A. G. Evans
Pierce Hall
29 Oxford Street

1 Harvard University
DEAS
Attn: Prof. John W. Hutchinson
Pierce Hall
29 Oxford Street
Cambridge, MA 02138

1 Hewlett-Packard
Attn: Jason Sun
MS 1013A
1000 N. E. Circle Blvd.
Corvallis, OR 97333

1 Hysitron Inc.
Attn: Sean Corcoran
2010 E. Hennepin Ave.
Minneapolis, MN 55413

1 Hysitron Inc.
Attn: Tom Wyrobek
2010 E. Hennepin Ave.
Minneapolis, MN 55413

1 IBM Research Division
T. J. Watson Research Center
Attn: R. F. Cook
P. O. Box 218
Yorktown Heights, NY 10598

1 Intel Components Corporation
Attn: Harry Fujimoto
3065 Bowers Ave
P. O. Box 58126
Santa Clara, CA 95052-8126

1 Intel Components Corporation
Attn: Qing Ma
3065 Bowers Ave
Santa Clara, CA 95052

1 Intel Components Corporation
Attn: Gabi Neubauer
3065 Bowers Ave
P. O. Box 58119
Santa Clara, CA 95052-8119

1 Johns Hopkins University
Materials Science and Engineering
Attn: T. P. Weihs
102 Maryland Hall
3400 N. Charles Street
Baltimore, MD 21218-2689

1 Kanazawa Institute of Technology
Advanced Materials Science Research and Development Center
Attn: Eiji Kusano
3-1 Yatsukaho Matto Ishikawa 924-0838
Japan

1 Lawrence Berkeley Laboratory
Attn: R. Cannon
MS 62-203
Berkeley, CA 94720

1 Lawrence Berkeley Laboratory
Attn: A. W. Thompson
One Cyclotron Road
MS 62-203
Berkeley, CA 94720

1 Linkoping University
Department of Physics
Attn: Dr. L. Hultman
Thin Film Division
Linkoping
Sweden S-581-83

1 Louisiana State University
Department of Mechanical Engineering
Attn: Stathis Meletis
Baton Rouge, LA 70803-6413

1 Max-Planck Institut fur Eisenforschung
Max-Planck Str. 2
Attn: Dr. Peter Neumann
4000 Dusseldorf
Postfach 140 444
Germany

1 Michigan State University
Metallurgy, Mechanics, and Materials
Attn: James P. Lucas
A317 Engineering Building
East Lansing, MI 48824-1226

1 Motorola
Attn: Indira Adhihetty, MS 360
2200 W. Broadway
Mesa, Arizonia 85202

1 MSME
Attn: R. O. Ritchie
467 Evans Hall
Berkeley, CA 94720-1760

1 Nano Instruments, Inc.
Attn: Barry Lucas
1001 Larson Dr.
Oak Ridge, TN 37830

1 Nano Instruments, Inc.
Attn: Michael O'Hern
1001 Larson Dr.
Oak Ridge, TN 37830

1 Nano Instruments, Inc.
Attn: Warren Oliver
1001 Larson Dr.
Oak Ridge, TN 37830

1 National Institute of Standard & Technology
Materials Science and Engineering
Attn: Tim Foecke
Bldg. 223 / Rm 309
Gaithersburg, MD 20899

1 National Institute of Standard & Technology
Ceramics Division
Attn: Ralph Krause
Gaithersburg, MD 20899

1 National Institute of Standard & Technology
Ceramics Division
Attn: Doug Smith
Gaithersburg, MD 20899

1 Ohio State University
Materials Science and Engineering
Attn: Peter Anderson
2041 College Road
Columbus, OH 43210-1179

1 Oxford University
Department of Materials
Attn: Prof. Adrian Sutton
OX1 3PH
United Kingdom

1 Pennsylvannia State University
Attn: Wilfred Otano-Rivera
263 Materials Research Laboratory
University Park, PA 16802

1 Politechnico di Torino
Structural Mechanics
Attn: Prof. Alberto Carpinteri
1-10129 Torino
Italy

1 Read-Rite Corporation
Attn: Hsin-Fu Wang
44100 Osgood Road
Fremont, CA 94539

1 Rice University
Mechanical Engng and Materials Science
Attn: Prof. George M. Pharr, MS 321
6100 Main Street
Houston, TX 77005-1892

5 Seagate Technologies
Attn: James E. Angelo
8001 East Bloomington Fwy
Bloomington, MN 55420

1 Seagate Technologies
Attn: Joel Hoehn
7800 Computer Avenue South
Minneapolis, MN 55435

1 Southwest Research Institute
Attn: Kwai S. Chan
P. O. Box 28510
San Antonio, TX 78238

1 Southwest Research Institute
Attn: David Davidson
P. O. Box 28510
San Antonio, TX 78238

1 St. Petersburg State University
Department of Elasticity
Russian Academy of Sciences
Attn: Dr. Nikita Morozov
Bibliotechnaya 2
Stary Petershof
198904 St. Petersburg
Russia

1 Stanford University
Department of Materials Science and Engineering
Attn: Prof. John Bravman
Peterson Lab B550 #555-D
Stanford, CA 94305-2205

1 Stanford University
Department of Mechanical Engineering
Attn: Huajin Gao
265 Durand
Stanford, CA 94305-4040

1 Stanford University
Materials Science and Engineering
Attn: Erica Lilleoden
Peterson Lab B550
Stanford, CA 94305-2205

1 Stanford University
Materials Science and Engineering
Attn: Prof. William D. Nix
Peterson Lab B550
Stanford, CA 94305-2205

1 UES
Materials Research Division
Attn: Dr. Bhaskar S. Majumdar
4401 Dayton-Xenia Rd.
Dayton, OH 45432-1894

1 University of Calgary
Department of Mechanical Engineering
Attn: Scott X. Mao
2500 University Dr. N.W.
Calgary, AB
Canada T2N 1N4

1 University of California, Los Angeles
Mechanical and Aerospace Engineering
Attn: Prof. Nasar Ghoniem
46-1476 Enginnering IV
Los Angeles, CA 90095-1597

1 University of California, Santa Barbara
Materials Department Engineering III
Attn: D. R. Clarke
Santa Barbara, CA 93106

1 University of California, Santa Barbara
Materials Department Engineering III
Attn: M. Y. He
Santa Barbara, CA 93106

1 University of California, Santa Barbara
Department of Mechanical Engineering
Attn: Prof. Zhigang Suo
Santa Barabara, CA 93106

1 University of Illinois
Theoretical and Applied Mechanics
Attn: Prof. K. J. Hsia
104 South Wright Street
216 Talbot Laboratory
Urbana, IL 61801-2935

1 University of Illinois
Theoretical and Applied Mechanics
Attn: Prof. J. K. Shang
216 Talbot Laboratory
104 South Wright Street
Urbana, IL 61801-2935

1 University of Michigan
Materials Science and Engineering
Attn: Prof. Ronald Gibala
2026 Dow Building
2300 Hayward Street
Ann Arbor, MI 48109-2136

1 University of Michigan
Materials Science and Engineering
Attn: Prof. Wayne Jones
2026 Dow Building
2300 Hayward Street
Ann Arbor, MI 48109-2136

1 University of Michigan
Department of Mechanical Engineering and Applied Mechanics
Attn: Michael D. Thouless
Ann Arbor, MI 48109

1 University of Michigan
Nuclear Engng and Radiological Sciences
Attn: Gary S. Was
Cooley Building
2355 Bonisteel Blvd.
Ann Arbor, MI 48109-2104

10 University of Minnesota
CEMS
Attn: William W. Gerberich
151 Amundson Hall
421 Washington Ave SE
Minneapolis, MN 55455

1 University of Minnesota
CEMS
Attn: Mike Kriese
151 Amundson Hall
421 Washington Ave SE
Minneapolis, MN 55455

1 University of Newcastle
Materials Division
Attn: Prof. Trevor F. Page
Herschel Building
Newcastle NE1 7RU
United Kingdom

1 University of Oxford
Department of Materials
Attn: Prof. John B. Pethica
Parks Road
Oxford OX1 3PH
United Kingdom

1 University of Oxford
Department of Materials
Attn: Prof. S. G. Roberts
Parks Road, Oxford
OX1 3PH
United Kingdom

1 University of Rochester
Department of Mechanical Engineering
Attn: S. J. Burns
Materials Science Program
Rochester, NY 14627-0133

1 University of Rochester
Department of Mechanical Engineering
Attn: James C. M. Li
Rochester, NY 14627

1 University of Saarland
Department of Materials Science
Attn: Prof. Horst Vehoff
Building 43B
P. O. Box 151150
D-66041 Saarbrucken
Germany

1 University of Virginia
Materials Science and Engineering
Attn: R. P. Gangloff
Thornton Hall
Charlottesville, VA 22903-2492

1 University of Virginia
Materials Science and Engineering
Attn: John Scully
Thornton Hall
Charlottesville, VA 22903-2492

1 University of Washington
Attn: Prof. Rene Overney
Department of Chemical Engineering
P. O. Box 351750
Seattle, WA 98195-1750

1 Washington State University
Mechanical and Materials Engineering
Attn: Dave Bahr
P. O. Box 642920
Pullman, WA 99163

1 Washington State University
Dept. of Mechanical and Materials Engineering
Attn: Richard Hoagland
Pullman, WA 99164-2920

1 Jeffrey S. Zabinski
WL/MLBT Bldg. 654
2941 P. St. Ste. 1
WPAFB, OH 45433

1	MS 0333	Jill Glass, 1833
1	MS 0333	Sandy Monroe, 1833
1	MS 0333	Alan Hurd, 1841
1	MS 0340	Wendy Cieslak, 1832
1	MS 0342	Dick Salzbrenner, 1805
1	MS 0437	E. D. Reedy, Jr., 9118
1	MS 0533	Dale Lyngen, 2343
1	MS 0958	John Emerson, 1472
1	MS 0959	Robert L. Poole, 1471
5	MS 0959	D. P. Norwood, 1471
1	MS 1081	Ken Peterson, 1275

1	MS 1413	Jack Houston, 1114
1	MS 1413	Terry Michalske, 1114
1	MS 1423	Maarten de Boer, 1114
1	MS 9001	T. O. Hunter, 8000 Attn: J. B. Wright, 2200 M. E. John, 8100 L. A. West, 8200 W. J. McLean, 8300 R. C. Wayne, 8400 P. N. Smith, 8500 P. E. Brewer, 8600 L. A. Hiles, 8800 D. L. Crawford, 8900
1	MS 9161	R. Q. Hwang, 8716
1	MS 9402	Doug Medlin, 8715
1	MS 9403	M. I. Baskes, 8712
10	MS 9403	N. R. Moody, 8712
1	MS 9405	M. T. Dyer, 8700 Attn: C. M. Hartwig, 8701 J. C. F. Wang, 8713 G. J. Thomas, 8715 K. L. Wilson, 8716 S. M. Foiles, 8717 E.-P. Chen, 8742 P. E. Nielan, 8743 W. A. Kawahara, 8746
3	MS 9018	Central Technical Files, 8940-2
4	MS 0899	Technical Library, 4414
1	MS 9021	Technical Communications Dept., 8815/Technical Library, MS0899, 4414
2	MS 9021	Technical Communications Dept. 8815, for DOE/OSTI